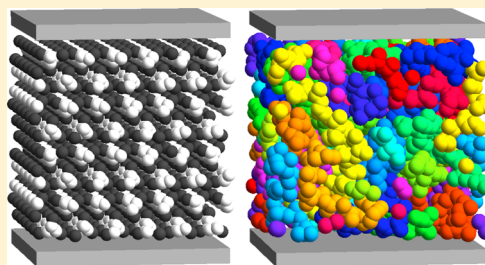


Calculated Interfacial Free Energies and Heterogeneous Nucleation of Isotactic Polypropylene

Michael P. Howard* and Scott T. Milner

Department of Chemical Engineering, The Pennsylvania State University, University Park, Pennsylvania 16802, United States

ABSTRACT: The surface free energy of crystalline isotactic polypropylene (iPP) and the interfacial free energy of crystalline iPP with a featureless Hamaker constant matched surface are determined by an all-atom lattice dynamics method including contributions from phonons treated quantum-mechanically and analytical “tail corrections” for long-ranged dispersion forces. The relative magnitudes of quantum effects, tail corrections, and finite system size effects on the surface free energy are assessed. The surface tension of iPP melt and the interfacial tension of iPP melt with a featureless substrate are determined from all-atom molecular dynamics simulations. We apply these results to a heterogeneous “cylindrical cap” nucleus on a featureless substrate, for which a contact angle of $79^\circ \pm 3^\circ$ is found. This value is in reasonable agreement with analysis of quiescent crystallization of commercial iPP samples, and thus lends support to the cylindrical cap model for heterogeneous nucleation.



INTRODUCTION

In typical polymer crystallization processes, bulk melts are quenched to temperatures below the melting point where the polymer can nucleate and crystallize. Homogeneous nuclei form within the melt, while heterogeneous nuclei form on surfaces and interfaces. The presence of these interfaces reduces the heterogeneous nucleation barrier relative to the homogeneous barrier, and hence softens the temperature dependence of the heterogeneous nucleation rate compared to purely homogeneous nucleation. At typical quench temperatures for isotactic polypropylene (120–140 °C), heterogeneous nucleation tends to dominate.¹

In a companion publication, we have proposed a simple “cylindrical cap” model for heterogeneous nucleation of isotactic polypropylene (10.1021/ma400702q). The key controlling parameter in this model is the contact angle of the cap with a featureless Hamaker constant matched surface. As shown in Figure 1, the contact angle θ arises from a balance

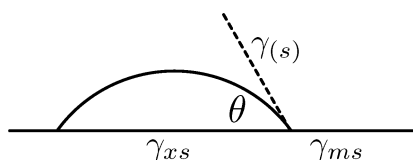


Figure 1. Cross section of cylindrical cap nucleus with featureless surface.

between the interfacial tension of the lateral face of the nucleus with the melt $\gamma_{(s)}$, the interfacial free energy of the crystal with the substrate γ_{xs} , and the interfacial tension of the melt with the substrate γ_{ms} .

We have extracted a value for the contact angle ranging from roughly 40° to 70° from experimental data (10.1021/ma400702q). One way to lend support to this model is to

calculate a value for the contact angle from theory, and compare it to the experimental value. Although we have previously estimated a value for $\gamma_{(s)}$, experimental data is not available for γ_{xs} and γ_{ms} , and it is difficult to make estimates for these values. A more convenient way to calculate γ_{xs} is by a lattice dynamics all-atom calculation of the interfacial free energy of the crystal against a model surface. The melt-substrate interfacial tension γ_{ms} can be calculated from a molecular dynamics simulation. With all three interfacial energies known, Young's equation can be applied to estimate the contact angle.

Lacks and Rutledge have applied the quasi-harmonic lattice dynamics method to compute thermodynamic properties of polymer crystals from an atomistic Hamiltonian, including the effects of thermal fluctuations. In their method, the total free energy of a small system of atoms is minimized at finite temperature by assuming all chains in the unit cell are identical, and adjusting their relative positions and orientations, as well as the lattice parameters. Entropic effects are included through quantum vibrations of the crystal, assuming a harmonic oscillator model. Phonon band structures are computed by applying Bloch's theorem, and then constructing and numerically integrating over the first Brillouin zone on a mesh of wave vectors. Analytical derivatives are used to compute forces, and Ewald summation is used to treat “long-ranged” dispersion interactions. Lacks and Rutledge have computed the temperature dependence of mechanical properties of bulk crystalline polyethylene and isotactic polypropylene, including thermal expansion coefficients and elastic moduli.^{2,3} The quasi-harmonic approximation was found to be valid up to roughly one-half to two-thirds of the melting point, at which point

Received: April 4, 2013

Revised: July 11, 2013

Published: August 9, 2013



anharmonic coupling effects were found to cause significant deviations.⁴

Using this approach, Wilhelmi and Rutledge have computed the surface free energy of crystalline polyethylene at finite temperature.⁵ They obtained the surface free energy by comparing the free energy of a slab and a bulk crystal, again adjusting parameters to minimize the total free energy of the systems. They studied a system that was several unit cells wide in the slab dimension (roughly 50 Å), and again applied Bloch's theorem to the unit cell in the periodic dimensions to compute a 2D Brillouin zone for calculating the vibrational free energy. They were unable to use Ewald summation methods for the dispersion interactions because of the two-dimensional slab geometry, and instead capitalized on the translational periodicity of the crystal to apply a large unit-cell based cutoff radius of 25 Å.

In this work, we employ the simpler harmonic method to estimate γ_{xs} . In the harmonic approximation, the lattice parameters are held constant, and all calculations are carried out using the energy minimized structure at 0 K neglecting the effect of zero point energy. As observed in ref 2, zero point energy has a negligible effect on the 0 K lattice parameters for bulk crystals. Although it is expected that the harmonic approximation incurs larger errors than the quasi-harmonic approximation at finite temperature, at present it is our goal only to estimate a contact angle for a nucleus by estimating the interfacial free energy γ_{xs} , and not to obtain precise values for properties at finite temperature. For this reason, we accept the limitations of the harmonic approximation in order to greatly simplify the process of optimizing the crystal structure.

We expand on the method used by Wilhelmi and Rutledge for polyethylene in two important ways: (1) the inclusion of an index matched substrate for the crystal and (2) the inclusion of tail corrections rather than increased cutoff radius to simulate "infinite" systems. We are unaware of others that have simulated the interfacial free energy of a crystal against a substrate toward an understanding of polymer nucleation.

Furthermore, with the advantage of modern computing power, we have undertaken to simulate a considerably larger system than was accessible to Wilhelmi and Rutledge. Simulating a large system has the advantage that vibrations can be treated more simply in real space rather than through the application of Bloch's theorem and integration over the Brillouin zone. Zhao et al. have shown for several properties of silicon (including the thermal expansion coefficient) that the values obtained from a real space calculation with only a few unit cells of atoms are virtually indistinguishable from the reciprocal space calculation with Brillouin zone integration.⁶ However, large systems also present new difficulties. Analytical derivatives and large cutoff radii become computationally impractical. Instead, we can use analytical "tail corrections" unique to the slab geometry to calculate potential energies for infinite crystals and semi-infinite slabs from results obtained with finite cutoffs.

The surface tension of a liquid interface can be calculated from a molecular dynamics simulation. We apply the theory of Kirkwood and Buff to calculate the surface tension for melt polypropylene from the pressure anisotropy, which is an easily accessible quantity in simulation.⁷ As is true for the crystal, dispersion forces can contribute to the surface tension significantly. Analytical tail corrections developed by Chapela et al. and corrected by Alejandre et al. and Blokhuis et al. are applied to the simulation results to account for the long-ranged

dispersion forces.^{8–10} The same principles can be applied to a liquid–solid interface, and we employ this method to calculate the melt–substrate interfacial tension γ_{ms} .

In this work we consider the interfaces of four systems: crystal–vacuum, melt–vacuum, crystal–substrate, and melt–substrate. For the crystal–vacuum interface, we estimate the surface free energy of the crystal, and assess the relative contributions of quantum effects, tail corrections, and finite system sizes. We calculate a value for the surface tension of polypropylene from the melt–vacuum interface and compare it to experimentally determined values. For the crystal–substrate interface, we again calculate the interfacial free energy, and combine it with a result for the interfacial tension of the melt–substrate interface to estimate a value for the contact angle of a cylindrical cap heterogeneous nucleus against a Hamaker-matched surface.

CRYSTAL COMPUTATIONAL METHODS

Interfacial energies of solids arise due to differences in free energy between bulk systems and slab systems with interfaces. The free energy has a potential energy contribution from bonded and nonbonded interactions, as well as an entropic contribution due to vibrations. Intuitively, it is expected that the potential energy of the crystal against the surface should be higher compared to the bulk crystal due to missing Lennard-Jones contacts, but the vibrational free energy should be slightly lowered due to the increased vibrational freedom of atoms near the surface.

To calculate the interfacial free energy, consider a process starting from a bulk crystal and a bulk substrate. Work is done to break both bulk structures into two semi-infinite half planes, separating the planes from contact in vacuum. Two interfaces are then formed by bringing each plane of crystal into contact with the substrate. The interfacial free energy is then given by the Dupré equation¹¹

$$\gamma_{xs} = \gamma_x + \gamma_s + F_{xs} \quad (1)$$

where γ_x and γ_s are the surface free energies of the bulk crystal and substrate defined

$$\gamma_i = -\frac{1}{2}F_{ii} \quad (2)$$

and F_{ij} is the free energy of interaction per unit area of an interface between i and j obtained by bringing i and j from separation to contact. Note that the interaction energy is a free energy, which may include entropic contributions.

The surface free energy of the crystal γ_x is straightforward to calculate from the energies of a bulk crystal and a slab of crystal against vacuum

$$\gamma_x = -\frac{1}{2}F_{xx} = \frac{F_{\text{vac}} - F_{\text{xtal}}}{2A} \quad (3)$$

where F_{vac} and F_{xtal} are the Helmholtz free energies of the crystal slab with vacuum and the bulk crystal respectively, and A is the cross sectional area of the interface.

For a large slab of crystal between two substrate "wall" interfaces (such as the system shown in Figure 2), the energy of interaction is

$$F_{xs} = \frac{F_{\text{wall}} - F_{\text{vac}}}{2A} \quad (4)$$

where F_{wall} is the free energy of the system with walls, and the factor of 2 accounts for the presence of two interfaces.

The complete expression for the surface tension is then

$$\gamma_{xs} = \frac{F_{\text{wall}} - F_{\text{xtal}}}{2A} + \gamma_s \quad (5)$$

We will discuss methods for estimating γ_s later. Note that if the substrate is vacuum (and hence γ_s is zero, and F_{wall} can be replaced by F_{vac}), eq 5 reduces to eq 3.

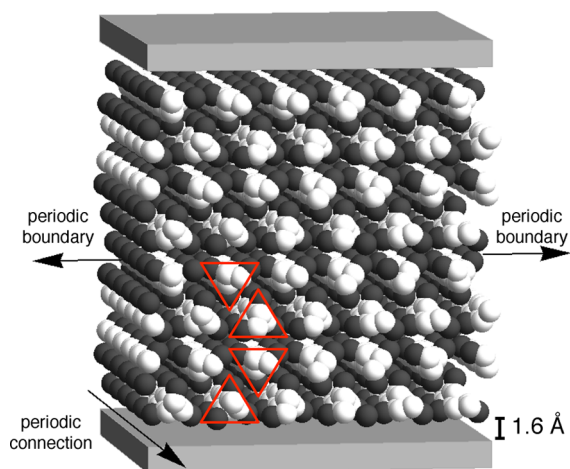


Figure 2. Simulation box for crystal slab against Hamaker matched surface. White atoms indicate backbone carbons while black atoms indicate methyl carbons (hydrogen atoms not depicted). Carbon atoms are 75% space filling. Triangles outline four chains in a unit cell.

Normal Mode Analysis. The harmonic approximation is a reasonable model for the vibrational free energy. The Hamiltonian is expanded to quadratic order in displacement from the 0 K minimum energy configuration. This expansion has a set of normal eigenmodes with frequency ω_i , which decouple the vibrations to a set of independent harmonic oscillators. An N atom bulk crystal will have $3N - 3$ normal modes, since there will be three zero-modes corresponding to bulk translation of the system. For a crystal against a substrate, there will be $3N - 2$ normal modes because one direction of translational invariance is lost normal to the substrate.

It is important to treat the normal modes quantum mechanically because many have energy much larger than kT . The vibrational free energy F_v is then

$$F_v = \sum_i \frac{\hbar\omega_i}{2} + \frac{1}{\beta} \sum_i \ln(1 - e^{-\beta\hbar\omega_i}) \quad (6)$$

where $\beta = 1/kT$. The total free energy F is given by adding the potential minimum U_0 to the vibrational energy F_v .

Ideally, we would perform calculations with an infinite (or nearly infinite) crystal. However, this is infeasible for numerical reasons. Computation of the normal modes has unfavorable scaling with the number of atoms. One way to represent the infinite crystal with a finite number of atoms is to treat the normal modes in reciprocal (\mathbf{k}) space. Given that the crystal is translationally periodic, the atomic positions of a single unit cell can be used to represent the infinite crystal by applying Bloch's theorem to the atomic displacements, as has been done by Wilhelmi and Rutledge for polyethylene.⁵ The reciprocal space calculation has the advantage that only a small number of atoms needs to be used to calculate the normal modes. The normal modes then become a function of wave vector $\omega_i(\mathbf{k})$, and the free energy is obtained by modifying eq 6 to sum over wave vectors. Since the infinite crystal will have an infinite set of wave vectors, and a unique set of wave vectors is determined by the first Brillouin zone, this summation can be replaced by an integration over the first Brillouin zone. This integration is typically performed by numerically integrating on a mesh of wave vectors.

A simpler, although potentially less accurate, way to compute the normal modes for an infinite crystal is to construct a supercell (system of multiple unit cells) in real space. Since the supercell contains many unit cells, computing all the normal modes of the supercell is equivalent to sampling many wave vectors in reciprocal space. In principle, the supercell calculation omits modes present in the infinite crystal that span multiple supercells and would be included by integrating the first Brillouin zone, and so some error is introduced by this approximation. However, since the size of the first Brillouin zone is inverse to the size of the supercell, for a sufficiently large system the

first Brillouin zone collapses to a point, the real space and reciprocal space results converge, and negligible error is introduced by omitting the integration.⁶

Real space normal modes are computed for an atomistic-level model by thorough energy minimization of the supercell followed by the construction and diagonalization of the mass-weighted Hessian matrix of the potential. The eigenvalues of the Hessian can then be converted to normal-mode frequencies. We use the OPLS-aa force field for our molecular Hamiltonian, and capabilities of the GROMACS simulation package for energy minimization, Hessian construction, and diagonalization.^{12,13}

In this work, a supercell containing 72 unit cells will be employed for the real space calculation of the normal modes. It is difficult to quantify the error that is introduced by omission of the Brillouin zone integration. There is no readily apparent analytical or scaling argument for how the normal modes computed in real space and reciprocal space should converge due to the diagonalization step. The easiest way to verify that the normal modes are accurate is to check the convergence of a few properties, such as the free energy, by changing the number of atoms in the real space calculation. Unfortunately, there is an upper limit to the number of atoms that can be used in our calculations due to large memory requirements for the Hessian matrix, and we cannot reduce the size of the system without reducing the potential cutoff to insufficient lengths, and hence changing the Hamiltonian. Instead, we remain optimistic that we have constructed a sufficiently large unit cell, and we may consider the omission of the Brillouin zone integration for the supercell as an approximation.

We note that the harmonic approximation may introduce significant error at high finite temperature due to two effects. The harmonic approximation does not include effects from the thermal expansion of the lattice. The quasi-harmonic approximation, as employed by Lacks and Rutledge, includes these effects, and is more accurate at finite temperature. Error is also introduced in both the harmonic and quasi-harmonic approximation by anharmonic coupling between modes at high finite temperature.⁴ However, for our present purposes of estimating γ_{ss} and a contact angle, the harmonic approximation can be considered a reasonable first estimate.

Crystal Tail Corrections. Intermolecular van der Waals forces dominate the attractive forces in a crystal. Since these forces are relatively short-ranged (decaying as r^{-6}), the typical approach in calculations with atomistic classical Hamiltonians (as in molecular dynamics simulations) is to enforce a cutoff on the order of a nanometer in order to improve efficiency. The resulting truncation errors in the force on a given atom are typically quite small. However, in quantities such as the potential energy, missing weak attractions from many distant atoms can add up to a significant difference.

The truncation effect is important when comparing the free energy of a bulk crystal to the free energy of a crystal slab. Although both the bulk crystal and the slab are missing cohesive energy beyond the cutoff, the slab is not missing as much energy because part of the space beyond the cutoff is vacuum. This means that the apparent potential energy of the bulk crystal is much higher than its true value, while the apparent potential energy of the slab is only somewhat higher. This artificially reduces the difference in potential energy between the slab and bulk, which favors the formation of interfaces and causes the apparent surface energy to be lower than its true value.

To remedy this, we introduce analytical tail corrections for the van der Waals interactions, in which missing attractive energy beyond the cutoff is added back, approximating the missing atoms as a featureless continuum with the same density as the system. The Lennard-Jones 12–6 potential is

$$U(r_{ij}) = 4\epsilon_{ij} \left(\frac{\sigma_{ij}^{12}}{r_{ij}^{12}} - \frac{\sigma_{ij}^6}{r_{ij}^6} \right) \quad (7)$$

where r_{ij} is the interatomic distance, and ϵ_{ij} and σ_{ij} have their usual meanings. A typical cutoff radius is approximately $2.5\sigma_{ij}$. Beyond this distance, the fully periodic system can be approximated as a structureless continuum.¹⁴ Integrating eq 7 beyond the cutoff sphere gives the “missing” potential energy U_{sph} of an atom of type i

interacting with a density of type j in the fully periodic crystal (Figure 3a)

$$U_{\text{sph}}(r_c) = \frac{\rho_j}{2} \int_{r_c}^{\infty} dr_{ij} U(r_{ij}) 4\pi r_{ij}^2 \quad (8)$$

$$= 8\pi\rho_j\epsilon_{ij} \left[\frac{\sigma_{ij}^{12}}{9r_c^9} - \frac{\sigma_{ij}^6}{3r_c^3} \right] \quad (9)$$

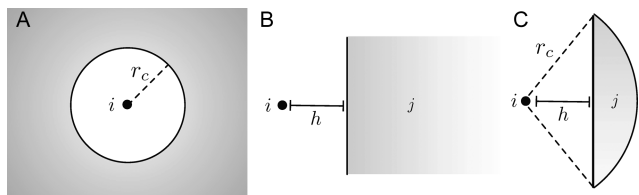


Figure 3. Schematics of integrals for tail corrections. (A) Spherical correction $U_{\text{sph}}(r_c)$. (B) Half plane correction $U_{\text{half}}(h)$. (C) Cap correction $U_{\text{cap}}(r_c, h)$.

where r_c is the cutoff radius and ρ_j is the number density of the j th atom type. The full tail correction is given by summing over all atoms interacting with all possible density types.

This method applies well to the full crystal, which has fully periodic boundary conditions in all directions (i.e., uniform composition). However, it fails when an atom is not surrounded by a repeating structure with the same composition (for example, if there is a gap or surface in one direction as is the case for a crystal slab). The correction in eq 9 would artificially “credit” missing interactions in the void where no atoms exist.

Instead, the missing energy between an atom of type i and a density of type j must be found by integrating over only the volume of the slab beyond the cutoff radius (V_c), which is infinite in two dimensions and finite in a third

$$\Delta U_{ij} = \frac{\rho_j}{2} \int_{V_c} d\mathbf{r}_{ij} U(|\mathbf{r}_{ij}|) \quad (10)$$

where \mathbf{r}_{ij} represents the vector between the atom and the density. If the system is homogeneous beyond the cutoff, eq 10 is equivalent to eq 8. This integral is not trivial to compute directly, but can instead be conveniently evaluated by manipulating simpler integrals. The general correction scheme is to add back the energy missing from the slab beyond the cutoff (as for the bulk crystal), but then subtract the energy that was artificially credited to the gapped dimension (where there is no crystal).

The tail correction for an atom of type i that is a distance h_1 and h_2 ($h_1 \leq h_2$) from the edges of slab of thickness $2d$ with cutoff radius r_c ($\leq d$) is

$$\Delta U_{ij} = \begin{cases} U_{\text{sph}}(r_c) - U_{\text{half}}(h_1) - U_{\text{half}}(h_2) & h_1 \geq r_c \\ U_{\text{sph}}(r_c) - U_{\text{half}}(h_1) - U_{\text{half}}(h_2) & h_1 < r_c \\ \quad + U_{\text{cap}}(r_c, h_1) \\ U_{\text{sph}}(r_c)/2 - U_{\text{half}}(2d) & h_1 = 0 \end{cases} \quad (11)$$

where j indicates the atom type interacting with an atom of type i . The full tail correction to the truncated potential is computed by summing over all atoms (each with a specific type i and edge distances) and then summing over all j atom types.

In eq 11, U_{half} is the tail correction for an atom of type i interacting with a semi-infinite half plane with density type j a distance h away (Figure 3b).

$$U_{\text{half}}(h) = 2\pi\rho_j\epsilon_{ij} \left[\frac{\sigma_{ij}^{12}}{45h^9} - \frac{\sigma_{ij}^6}{6h^3} \right] \quad (12)$$

U_{cap} is the tail correction for an atom of type i interacting with a spherical cap with density type j , defined by a sphere of radius r_c with nearest distance h (Figure 3c)

$$U_{\text{cap}}(r_c, h) = 4\pi\rho_j\epsilon_{ij} \left[\left(\frac{\sigma_{ij}^6}{3r_c^3} - \frac{\sigma_{ij}^{12}}{9r_c^9} \right) (1 - h_r) + \frac{\sigma_{ij}^{12}}{90h^9} (1 - h_r^{10}) - \frac{\sigma_{ij}^6}{12h^3} (1 - h_r^4) \right] \quad (13)$$

where $h_r = h/r_c$. Details of this derivation are included as an Appendix.

Crystal Finite Thickness Corrections. As discussed previously, although ideally we would analyze systems of infinite size, the number of atoms that can be simulated is restricted by the time and memory required to compute and diagonalize the Hessian matrix during the normal modes analysis. This is not problematic for the fully periodic crystal, since only a sufficiently large system and tail corrections are required to guarantee that the infinite crystal is well represented. However, we would like to compare the energy of the infinite crystal to the energy of an “infinite” slab (that is, a slab where each surface is unaware that the other exists). If the slab is not sufficiently thick, the slab “misses” cohesive energy from its middle, which artificially raises the surface tension. However, if the original slab is sufficiently large so that the normal modes are accurate, we can again correct this in the continuum.

The finite thickness correction to the interfacial free energy $\Delta\gamma_{\text{ss}}|_{ij}$ for atoms of type i in the slab of thickness $2d$ interacting with an atom of type j is

$$\Delta\gamma_{\text{ss}}|_{ij} = \frac{\pi}{2}\rho_i\rho_j\epsilon_{ij} \left[\frac{\sigma_{ij}^{12}}{90} \left(\frac{1}{d^8} - \frac{1}{(2d)^8} \right) - \frac{\sigma_{ij}^6}{3} \left(\frac{1}{d^2} - \frac{1}{(2d)^2} \right) \right] \quad (14)$$

where ρ_i is the number density of atoms of type i in the slab. We note that this finite thickness correction also applies to the slab-vacuum interface. Combining our simulation results with tail corrections and finite thickness corrections, we arrive at the final expression for the interfacial free energy of the crystal with a substrate from eq 5.

$$\gamma_{\text{ss}} = \left[\frac{\Delta U_0 + \Delta F_v}{2A} + \gamma_s \right] + \frac{\sum_{i,j}^{\text{slab}} \Delta U_{ij} - \sum_{i,j}^{\text{xtal}} U_{\text{sph}}(r_c)}{2A} + \sum_{i,j} \Delta\gamma_{\text{ss}}|_{ij} \quad (15)$$

The corrected interfacial free energy contains three groupings of terms: the “basic” interfacial free energy resulting directly from calculation with the truncated potential, the tail correction, and the slab finite thickness correction. ΔU_0 is the difference in the truncated potential energies, and ΔF_v is the difference in vibrational free energy between the slab and crystal systems computed from eq 6. Both the bulk crystal and the slab system have the same number of atoms. Tail corrections are taken by summing over all i atoms and all j atom types. Both sums on $\Delta\gamma_{\text{ss}}|_{ij}$ are taken over all possible atom types. Details of this derivation are included as an Appendix.

Crystal Structure. We have simulated the monoclinic α_1 (Cc) phase of isotactic polypropylene, as first described by Natta and Corradini.¹⁵ The α_1 phase has a unit cell consisting of four 3_1 helices with alternating handedness and all methyl groups pointing in the same upward or downward direction, as shown in Figure 4.

The α phase of polypropylene is polymorphic. It has been shown computationally that the α_2 ($P2_1/c$) phase is slightly more stable than the α_1 phase.¹⁶ In the α_2 phase, chains with two neighboring methyl groups have their methyls oriented in the same z direction, while chains with only one neighboring methyl group point in the opposite z

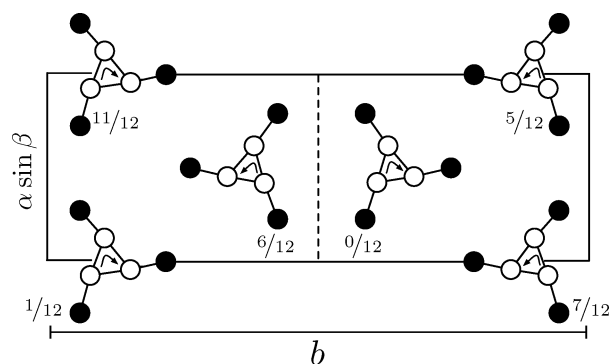


Figure 4. Projection of the α_1 phase of isotactic polypropylene into the $[a \sin \beta]$ – b plane. As in Figure 2, white circles represent backbone carbons, while black circles represent methyl groups. Arrows indicate handedness of chain. All methyl groups point in the same z direction. Fractional labels indicate vertical offset of methyl group in terms of fractions of one helical repeat. Dashed line indicates cleaved surface.

direction (for example, the middle two chains in Figure 4 would point upward if the outer two chains pointed downward). However, simulations by Ferro et al. and Corradini et al. have shown that the difference in potential energy of the α_1 and α_2 phases is marginal at best.^{17,18} Since the two phases have only minor differences in crystal structure and potential energy, the choice between α_1 and α_2 should have minimal effect on the calculated surface energy. For simplicity of system construction, we have chosen to simulate the α_1 phase.

In order to simulate surfaces, it is necessary to choose a plane upon which to cleave the crystal. We are interested in simulating the face that will have the lowest interfacial free energy, since it is expected that a nucleating crystal would naturally seek to minimize its surface energy. Wilhelmi and Rutledge found this to be the smooth (100) face for polyethylene in vacuum,⁵ and a similar result might be expected for the analogous (010) face for polypropylene in vacuum.

It is natural to ask if the same face will also minimize the free energy of the crystal with a substrate. By assumption, the substrate in our model is featureless and has no corrugation or templating to match the crystal. We can then reasonably conclude that the surface with the lowest free energy will be a “smooth” face since such a surface benefits most from lying adjacent to the substrate, which again corresponds to a smooth lateral surface. We have chosen to cleave the crystal at the (010) face as indicated by the dashed line in Figure 4.

Lattice Dynamics Calculations. All calculations were conducted using the GROMACS simulation package with the OPLS-aa force field and double precision methods for a system with 7,776 atoms.^{12,13} This system size corresponds to a supercell of six unit cells in the a direction, two unit cells in the b direction, and six helical repeats, for a roughly cubic box in Cartesian coordinates containing 72 unit cells.

Periodic boundary conditions and periodic covalent bonding were employed to represent an infinite system. Since chains were periodically bonded, an orthorhombic simulation box with chains appropriately shifted was used for simplicity. The crystal slab against vacuum was represented by adding a 10.0 nm gap to the crystal in fully periodic boundary conditions to isolate the slab in the gap dimension. The crystal against a substrate was modeled with two Lennard-Jones 9–3 walls (2D periodic boundary conditions) Hamaker constant matched to the crystal (Figure 2).

In the normal modes analysis, a switched 12–6 Lennard-Jones potential was employed for van der Waals interactions (cutoff from 1.0 nm, switched from 0.8 nm). Coulomb electrostatics were treated with a particle mesh Ewald (PME) method (short-range cutoff of 1.3 nm, dielectric constant $\epsilon = 2.3$) for the bulk crystal and crystal against vacuum.¹⁹ Coulomb interactions with a zero reaction field (cutoff from 1.0 nm) were used instead of PME for the crystal against the index matched surface, because PME is ill-suited for 2D periodic systems when the aperiodic dimension is not roughly three times the size of the periodic dimensions.¹²

The optimal lattice parameters for the crystal were found as follows. The backbone C–C–C angle was adjusted with the backbone dihedrals fixed in alternating trans–gauche angles (the idealized 3_1 helix) to minimize the potential energy of a single chain, which set the c parameter. The crystal was then constructed by placing appropriate copies and mirror images of the energy minimized chain in the structure identified by Natta and Corradini. The $a \sin \beta$ and b parameters were then adjusted to minimize the potential energy for the bulk crystal. The lattice parameters were assumed to be unchanged for the crystal–vacuum system. The wall spacing was adjusted to minimize the energy of the crystal–substrate system. Each system was then further minimized to a tolerance of 10^{-4} kJ/[mol nm] with the limited-memory Broyden–Fletcher–Goldfarb–Shanno (L-BFGS) quasi-Newton minimization algorithm, and the normal modes were computed. GROMACS returns the eigenvalues of the mass-weighted Hessian (λ_i) in units of kJ/[mol nm² amu]. The normal mode frequencies ω_i are then $(\lambda_i)^{1/2} \times 10^{12}$ s^{−1}.

After the normal modes analysis, the system potential energy was recalculated using a plain cutoff Lennard-Jones potential with the largest possible cutoff radius for both the Lennard-Jones and electrostatic interactions (1.9 nm). This cutoff also corresponds to half the slab thickness for the systems with interfaces, so eq 11 applies. Tail corrections and finite size corrections were then applied to this energy, and the interfacial free energy was computed according to eq 15.

Short isothermal–isobaric (NPT) molecular dynamics simulations were also conducted to check that the OPLS force field can reasonably reproduce experimental lattice parameters. The density was equilibrated at 1.0 atm and 300 K for 50.0 ps starting from the energy minimized structure. Switched Lennard-Jones and PME electrostatics (with the same parameters used for the normal modes analysis) were used with a velocity rescaling thermostat ($\tau = 0.1$ ps) and a Parrinello–Rahman barostat with anisotropic pressure coupling ($\tau = 1.0$ ps, $\kappa = 4.5 \times 10^{-5}$ bar^{−1}).²⁰ We found that at 300 K the average simulated lattice parameters were in excellent agreement with the experimental parameters also determined at room temperature, with a maximum error of 2.4% in the b parameter (see Table 1). On the basis of this, we can be fairly confident that the OPLS forcefield reasonably represents the real polypropylene crystal.

Table 1. Lattice Parameters of α_1 Isotactic Polypropylene from Experiment and our Simulations at 0 and 300 K (All Lengths in Å)

	experiment ¹⁵	OPLS 0 K	OPLS 300 K
a	6.65 ± 0.05	6.57	6.63
b	20.96 ± 0.15	19.40	20.46
c	6.50 ± 0.05	6.47	6.60
β	$99^\circ 20' \pm 1^\circ$	$99^\circ 36'$	$99^\circ 32'$

■ MELT COMPUTATIONAL METHODS

An expression for the melt–substrate interfacial tension γ_{ms} can be obtained analogously to eq 1.

$$\gamma_{ms} = \gamma_m + \gamma_s + F_{ms} \quad (16)$$

The dominant contributions to γ_m and F_{ms} are (as for the crystal) differing cohesive energies and (unlike the crystal) an entropic penalty for the motion of chains near the interface. The average melt–substrate interfacial tension γ_{ms} can then be calculated from the pressure anisotropy⁷

$$\gamma_{ms} = \frac{L_z}{2} \left\langle P_{zz} - \frac{1}{2}(P_{xx} + P_{yy}) \right\rangle + \gamma_s \quad (17)$$

$$= \gamma_{ms}^\circ + \gamma_s \quad (18)$$

where z is normal to the interface, L_z is the size of the simulation box in that direction, P_{ii} are the diagonal components of the pressure

tensor, and the factor of 2 accounts for the presence of two interfaces in the simulation box when a gap or substrate is introduced. It is convenient to evaluate the average in the canonical (NVT) ensemble with two Hamaker matched walls (as for the crystal).

We must explicitly add γ_s because the simulation does not account for the substrate in the pressure tensor. Although the melt is affected by the potential of the wall (and indeed “owns” all of the energy of the interaction), the substrate is “unaware” that it pays a penalty for the presence of the melt since the substrate atoms are not a part of the system. If no melt were present, the simulated surface tension would be zero. Hence, we must explicitly add the γ_s term to the simulated γ_{ms}° .

Melt Tail Corrections. As for the crystal, tail corrections due to dispersion forces can be significant for melt systems. Per the work of Chapela et al. and corrected by Alejandre et al. and Blokhuis et al.^{8–10} the tail correction can be computed by first fitting the density profile of the slab to a hyperbolic tangent

$$\rho(z) = \frac{1}{2}(\rho_1 + \rho_2) - \frac{1}{2}(\rho_1 - \rho_2) \tanh\left(\frac{z - z_0}{d}\right) \quad (19)$$

where ρ_1 and ρ_2 are the densities on either side of the planar interface centered at z_0 with nominal thickness d . It is typical to report the interface width in terms of the “10–90 thickness”, which is equal to $2.1972d$.²¹ The tail correction to the interfacial tension $\Delta\gamma_{ms}$ is then

$$\Delta\gamma_{ms} = 12\pi \sum_{i,j} \epsilon_{ij} \sigma_{ij}^6 (\rho_{i,1} - \rho_{j,2})^2 \times \int_0^1 ds \int_r^\infty dr \frac{3s^3 - s}{r^3} \coth\left(\frac{sr}{d}\right) \quad (20)$$

where the sum is taken on all possible pairings of atom types in the melt, and the subscripts on the density indicate the number density of a given atom type on either side of the interface, which can be obtained from ρ_1 and ρ_2 .

Molecular Weight Correction. An additional correction must be applied to the melt system to account for finite size effects of chains. Unlike the crystal, which was periodically bonded to itself and therefore representative of chains of infinite length, we are obliged to simulate polypropylene oligomers in the melt. In an all-atom calculation, these oligomers are limited to M_n orders of magnitude smaller than the typical M_n for commercial polypropylene. It has been shown that surface tension increases with M_n for many polymers.^{22–24} It has been noted that the surface tension scales as $M_n^{-2/3}$ for “low” molecular weights and as M_n^{-1} for “high” molecular weights.²³ The $M_n^{-2/3}$ dependence is a mostly empirical relation, usually attributed to solvent accessibility and surface-to-volume corrections for small molecules,^{24,25} while the M_n^{-1} dependence results from corrections for end effects that are applicable to many other properties of polymers.²⁶ The exact weight where this transition occurs is not well-defined, and to our knowledge has not been investigated for polypropylene. Data is not available for the surface tension of polypropylene versus molecular weight, presumably because of the difficulty of preparing a monodisperse sample. Instead, we will estimate a molecular weight correction for polypropylene based on the surface tension data available for the *n*-alkanes^{27,28} and polyisobutylene.²²

Suppose that the polymers of interest are large enough that the surface tension has a M_n^{-1} dependence. We might expect that the surface tension for similar polymers (such as polyethylene, polypropylene, and polyisobutylene, which differ only in the number of methyl backbone substituents) would have a similar dependence on “dimensionless” molecular weight, with the weight scaled appropriately to account for the different monomer weights for each. The natural choice is to scale the molecular weight by the weight of a Kuhn segment M_k

$$\gamma_m(M_n, T) = \gamma_m^\infty(T) \left(1 - c(T) \frac{M_k}{M_n}\right) \quad (21)$$

where M_n is the number-average molecular weight, γ_m^∞ is the surface tension of the chain of infinite molecular weight, and c is a dimensionless constant. Both the surface tension and the constant c may be functions of temperature.

A plot of $\gamma(M_n)$ versus $1/M_n$ for the higher weight alkanes and polyisobutylene at 297 K shows reasonably linear behavior (Figure 5).

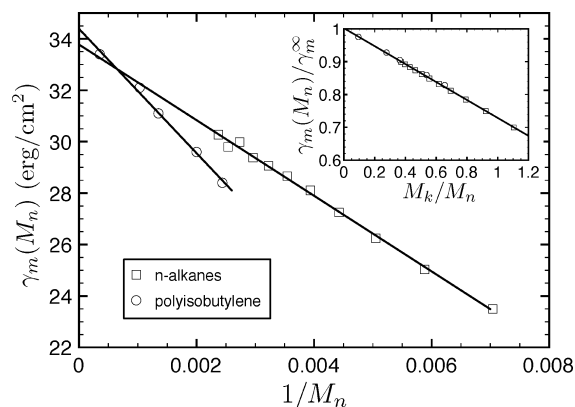


Figure 5. Surface tension of *n*-alkanes (ref 27) and polyisobutylene (ref 22) at 297 K. Inset shows data collapsed onto a master curve with intercept 1.0 and slope -0.28 .

The alkane series is plotted for $C_{10}H_{22}$ to $C_{30}H_{62}$. Lower weight alkanes (not plotted) show some curvature when plotted versus $1/M_n$, as has been noted elsewhere.²³ We note that the surface tension of polyisobutylene shows a better linear fit plotted versus M_n^{-1} than versus $M_n^{-2/3}$.

The Kuhn length is 14 Å for polyethylene, 11 Å for polypropylene, and 12 Å for polyisobutylene.^{29,30} One monomer in any of these polymers has a backbone length of roughly 2.5 Å in the all-trans configuration (we consider one monomer of polyethylene to be two CH_2 groups). Hence, the molecular weight of a Kuhn segment M_k is estimated to be 157 g/mol for polyethylene, 185 g/mol for polypropylene, and 269 g/mol for polyisobutylene.

Using these values for the weight of a Kuhn segment, the inset of Figure 5 shows the surface tensions for the *n*-alkanes and polyisobutylene at 297 K replotted in dimensionless form ($\gamma_m(M_n)/\gamma_m^\infty$ versus M_k/M_n). The data collapse well onto a linear curve that has a fitted intercept of approximately 1.0 as expected from eq 21, and gives a value for $c(297\text{ K})$ of 0.28.

The constant c may vary with temperature. Using data for the surface tension of the *n*-alkanes at 400 K gives a value of 0.40 for c .²⁷ Since only sparse data is available for the surface tension of polyisobutylene at high temperature for various molecular weight, we assume that c will remain the same for polypropylene and polyisobutylene at 400 K. Finally, in the absence of any available experimental data, we assume that the interfacial tension of the melt with the substrate will have the same dependence on molecular weight as for the surface tension of the melt.

The full expression for the melt-substrate interfacial tension is then

$$\gamma_{ms} = \frac{\gamma_{ms}^\circ(M_n) + \gamma_s + \Delta\gamma_{ms}}{1 - cM_k/M_n} \quad (22)$$

where $\gamma_{ms}^\circ(M_n)$ is the simulation result, c is 0.40 at 400 K, and M_k is the weight of a Kuhn segment of polypropylene (185 g/mol).

Molecular Dynamics Simulation. An all-atom simulation was performed in the GROMACS simulation package with the OPLS-aa force field and single precision methods. An equilibrated melt was prepared starting from a crystal containing 48 finite chains, each with 18 monomers (7872 total atoms), placed between two Hamaker constant-matched Lennard-Jones 9–3 walls (parameters the same as for the crystal calculations). The walls were moved out to introduce a large gap space for melting, and the crystal was partially melted with an NVT simulation at 500 K for 50.0 ns using a time step of 2.0 fs and a

velocity rescaling thermostat. The same parameters were used for the van der Waals interactions and electrostatics as were used for the normal mode analysis. The temperature was then adjusted down to 400 K, and the walls were manually brought back in as far as the system would allow. Because the directly simulated interfacial tension γ_{ms}^0 does not include any corrections or account for γ_s , the system favored the formation of interface. We capitalized on this to compress the melt between the walls using an NPT simulation at 1.0 bar and 400 K with semi-isotropic pressure coupling until the system had roughly cubic dimensions (about 4.5 nm). The melt was then allowed to equilibrate to its natural density in the cubic box with isotropic pressure coupling for 5.0 ns. Finally, to ensure complete melting, another 5.0 ns of NVT simulation at 400 K was conducted. In total, the melt was equilibrated for nearly 70.0 ns, and a visual inspection of the melt showed that the chains had adopted roughly random conformations.

The interfacial tension was then obtained from the pressure tensor for the melt-substrate interface with a 50.0 ns NVT simulation. The melt surface tension was also determined by removing the walls, introducing a 10.0 nm gap, switching to fully periodic boundary conditions, and collecting data over a 50.0 ns NVT simulation.

RESULTS AND DISCUSSION

Crystal–Vacuum Interface. The surface free energy of the lateral (010) face of polypropylene was found to be 80.0 erg/cm² at 0 K. Inclusion of the normal modes in the free energy had a significant effect on the surface energy. The normal modes contribute both a temperature independent zero-point term (the first term in eq 6), and a temperature dependent term to the free energy. The difference in zero-point vibrational free energy lowers the surface free energy by 8.9 erg/cm² at 0 K. Differences in the temperature dependent vibrational free energy of the bulk and the slab further lowers the surface energy at higher temperatures. Figure 6 shows the surface free energy extrapolated to typical crystallization temperatures from the harmonic approximation.

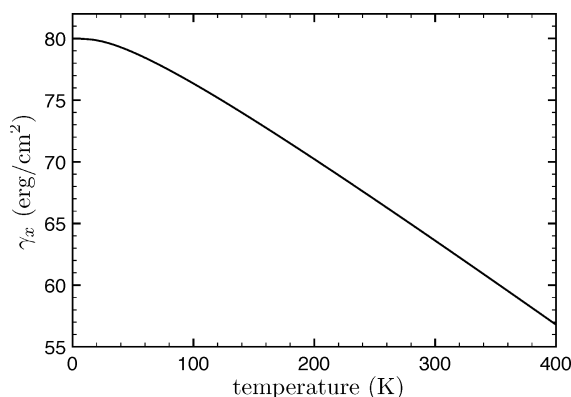


Figure 6. Surface free energy of (010) face of α_1 isotactic polypropylene.

The vibrational free energy significantly lowers the surface free energy (especially at finite temperature) because of a “softening” of vibrations near the surface of the slab crystal compared to the vibrations in the bulk, which increases the slab entropy. One way to visualize the effect of the soft surface vibrations is to examine the atomic displacements associated with each normal mode. Each normal mode has an associated eigenvector (of size $3N$), which can be partitioned into N triplets to give the atomic displacement vector $\Delta \mathbf{r}$ for each atom along the mass-weighted Cartesian coordinates. These atomic displacements point in the direction that each atom

would vibrate in the mode, and the norm of each displacement vector gives the amplitude of the motion. Large amplitudes indicate that the atom has more freedom to vibrate in any given mode. Since the position of each atom in the slab is known, we can compute the amplitude of motion for each atom as a function of distance from the nearest edge of the slab for a given mode. The nearest edge for the bulk crystal (which is fully periodic and has no real “edge”) was defined as the edge of the simulation box in the direction of the normal to the slab. We have then averaged these amplitudes over the two thousand lowest frequency modes, and plotted as a function of position in the slab (Figure 7).

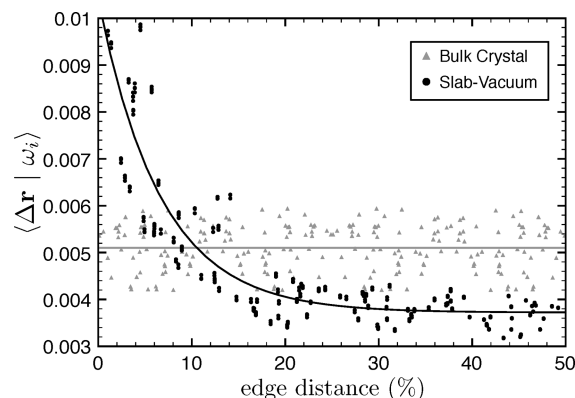


Figure 7. Average magnitude of the atomic displacements $|\Delta \mathbf{r}|$ for the first two thousand normal modes versus nearest edge distance for crystal–vacuum and bulk crystal systems. For the bulk crystal, the “edge” was defined as the simulation box size in the gap dimension.

As expected, the average magnitude of vibrations in the bulk crystal has essentially no spatial dependence. However, the magnitudes of vibrations within 10% of the nearest edge (roughly 4 Å) for the slab are considerably higher than those in the center of the slab. For higher frequency modes (not included in the average), the magnitudes show essentially no spatial dependence, just as for the bulk crystal. The two thousand lowest frequency modes for the crystal–vacuum system have lower frequency than the lowest frequency modes for the bulk system, which causes the crystal–vacuum system to have lower vibrational free energy. It is thus apparent that the vibrational free energy is lowered for the slab system due to increased vibrations by atoms near the surface in the lowest frequency lattice modes.

The tail corrections made a significant contribution to the surface energy. When the cutoff radius was increased from 1.0 nm for the normal modes analysis to 1.9 nm (the maximum cutoff radius possible in our periodic box), the surface energy increased by approximately 10.8 erg/cm². Continuum corrections beyond this cutoff added an additional 3.1 erg/cm² to the surface energy for a total correction of 13.9 erg/cm². This agrees with our expectations; increasing the cutoff radius and including tail corrections increases the total cohesive energy of the bulk system more than in the slab system since the tail corrections make atoms in the middle of the slab system “aware” that they are missing interactions that would be present in the bulk. Evidently, it is important to apply tail corrections when calculating surface energies in systems like organic crystals, where cohesive intermolecular attractions dominate.

The significant contribution of tail corrections to the potential invites the question: are the normal modes, which

are obtained from the Hessian of the potential, similarly sensitive to the missing tail energies? It would be unfortunate if the Hessian were significantly affected by cutoff effects, since further increasing the cutoff radius is impractical for numerical reasons. A cutoff radius of 1.0 nm is sufficiently large that (1) all important short-ranged interactions are treated discretely, and (2) all atoms are close to their “true” minimum energy positions. Then, we can analyze the effect of tail corrections on the normal modes by analyzing the magnitude of second derivatives of the tail corrections (see Appendix for details).

In the bulk system, the tail correction is a constant term that has no position dependence, so no correction to the Hessian is required. For the slab system, the tail corrections do depend on position, in the direction of the slab normal. Since the tail corrections are independent for each atom, this amounts to correcting only one-third of the diagonal elements of the Hessian. It can then be shown that the relative magnitude of these corrections compared to the Lennard-Jones contribution to the Hessian is of order $(\sigma/r_c)^5 \ll 1$. Thus, we can be reasonably confident that the normal modes are accurate.

The finite thickness corrections to the slab had only a small effect on the surface energy (-0.4 erg/cm²). This makes sense given that the simulated slab was already roughly 3.8 nm (eight molecular layers) wide. The slab was sufficiently thick that it was not “missing” a sizable amount of cohesive energy. On the basis of the small size of this correction, we can be reasonably confident that the normal modes in the slab system are representative of two isolated surfaces, and are not artificially softened by missing cohesive energy in the bulk of the slab. If this softened surface effect were present, we would be unable to remove it with a postsimulation correction. As an additional check, we have computed the density as a function of position in the slab, and found that it plateaus and adopts roughly bulk values in the middle of the slab. This suggests that the surfaces are indeed isolated.

Crystal–Surface Interface. The interfacial free energy of the crystal against the Hamaker-matched surface was found to be 39.5 erg/cm² at 0 K and 28.0 erg/cm² at 400 K (Figure 8).

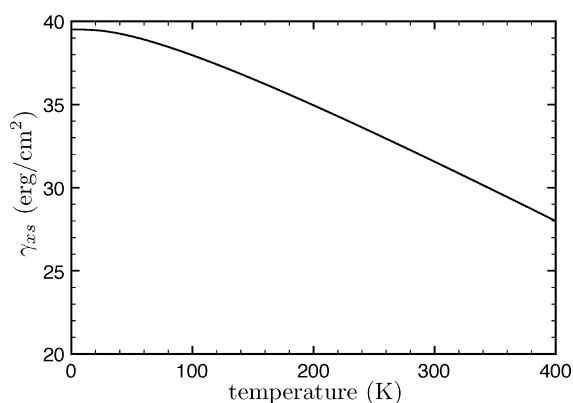


Figure 8. Interfacial free energy of (010) face of α_1 isotactic polypropylene with featureless Hamaker-matched substrate.

As expected, the interfacial free energy is considerably lower for the crystal–surface system than the crystal–vacuum system because the surface provides some cohesive interactions for the slab that the vacuum did not without significantly penalizing surface atoms entropically. The slab had a preferred distance from the surface of about 1.6 Å, which is in agreement with the rule of thumb of Israelachvili.³¹

Lattice mode vibrations for the slab with the Hamaker-matched substrate were not softened as much as for the slab with vacuum. This is evident in Figure 9, which visualizes this

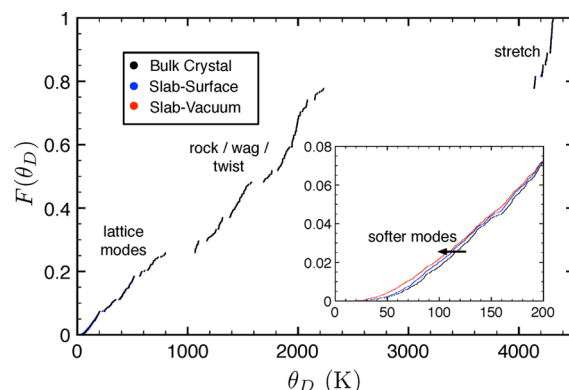


Figure 9. Cumulative fraction of normal modes below Debye temperature θ_D . Inset shows a closeup of the 0 to 200 K temperature range, where the phonons for the slab systems are shifted to be “softer”.

difference in the normal modes of the bulk and slab systems. The main figure shows the discrete cumulative fraction of normal modes F with energy less than or equal to a Debye temperature θ_D . Three distinct bands are observed: a low temperature band corresponding to lattice vibrations, a medium temperature band corresponding to the motion of the CH₂ groups, and a high temperature band corresponding to C–H bond stretching. The inset shows a close-up view of the low temperature modes for all three systems. The slab–vacuum curve is shifted to the left, which corresponds to having “softer” modes (modes with lower energy). The slab–surface system is also shifted left from the bulk crystal, but not by as much as the vacuum. This is because the presence of the substrate inhibits vibrations by atoms near the surface more than the vacuum interface.

At higher temperatures, the curves are not significantly shifted from one another, suggesting that the free energy is lowered mainly by the low frequency lattice modes. Although all modes contribute in principle to the zero-point vibrational free energy, only these low temperature lattice modes are “switched on” in the range of temperatures relevant to crystallization. Thus, it is the differences in these low temperature modes that dominate the reduction in the vibrational free energy of the slab systems versus the bulk crystal.

We have made two key approximations in our calculations of the crystal–surface interfacial free energy: (1) the surface is nonvibrating and Hamaker constant matched, and (2) the harmonic approximation may be used to estimate the surface energy at 400 K. We would physically expect that the presence of the crystal against the substrate should increase the vibrational free energy of the substrate since its entropy is reduced by surface adsorption. Treating this in our calculations would be quite difficult, since it requires exact knowledge of the structure of the substrate. Instead, we have calculated γ_s assuming only Lennard-Jones interactions between two semi-infinite half planes

$$\gamma_s = -\frac{1}{2}F_{ss}$$

$$= -\frac{1}{2}\left(\min_d \sum_{i,j}^{\text{types}} \pi \rho_i \rho_j \epsilon_{ij} \left[\frac{\sigma_{ij}^{12}}{90d^8} - \frac{\sigma_{ij}^6}{3d^2} \right] \right) \quad (23)$$

where the sum is taken over all possible pairs of atom types in the two half planes, and minimized with respect to the gap distance d between the slabs. For our substrate density, we obtain a value of 26.2 erg/cm² for γ_s . In light of our idealization of the substrate as a featureless surface, it is reasonable to approximate the surface as nonvibrating.

Previously, we have argued that the substrate should be roughly Hamaker constant matched to the crystal so that heterogeneities do not aggregate in the melt (10.1021/ma400702q). If the Hamaker constant of the substrate were to be slightly higher or slightly lower so that aggregation still does not occur, the interfacial free energy would change due to two competing effects. Increasing the density of the substrate increases the cohesive energy with the crystal, and hence reduces the interfacial energy. However, increasing this density also helps “stiffen” the vibrations of atoms near the surface, which reduces their entropy and hence increases the interfacial energy. These effects would be reversed if the density of the substrate were instead lowered. Evidently there is some optimal trade-off to be made here; however, without more detailed knowledge of the nucleating agents available in commercial melts, we believe that index matching the substrate to the crystal is a reasonable approximation.

Use of the harmonic approximation is a more sensitive issue. As discussed previously, the quasi-harmonic approximation is reasonably accurate to roughly one-half to two-thirds of the melting point (or about 200–300 K). We expect that the harmonic approximation would incur more error than the quasi-harmonic approximation, and that some error is also introduced by anharmonic coupling, especially at the temperature of interest (400 K). Our present goal is to estimate the contact angle of the crystal nucleus against a surface, and not to obtain precise values for the free energy or other properties at finite temperature. We contend that the harmonic approximation is roughly valid for this purpose.

Melt Interfaces. Figure 10 shows the time averaged density of the melt–vacuum and melt–substrate systems versus position in the slab. Both profiles have a large plateau in the middle,

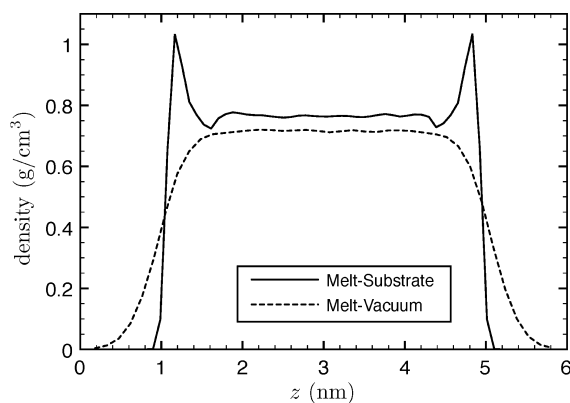


Figure 10. Melt density profiles for substrate and vacuum interfaces normal to interfaces. Note the sharpness of the substrate interface compared to the vacuum interface.

suggesting that the two interfaces are isolated from each other. The melt–vacuum interface is smooth, and can be well fit by eq 19. The melt–substrate interface is considerably sharper than the melt–vacuum interface, and exhibits significant ringing near the interfaces. Although this profile is not well-described by the hyperbolic tangent profile, we approximate the fit using eq 19 for purposes of computing the tail correction. Such a fit slightly overshoots the density in the middle of the slab and undershoots the edge ringing. Given that the ringing is narrow, we expect that these errors should roughly cancel each other when averaged by integration over the slab.

The 10–90 thickness of the melt–substrate thickness is only about 1.0 Å, while the melt–vacuum interface is roughly a more typical 7.2 Å.^{9,32} The sharpness of the melt–substrate interface is visually apparent on inspection of representative configurations for each system (Figure 11). The melt formed a nearly flat

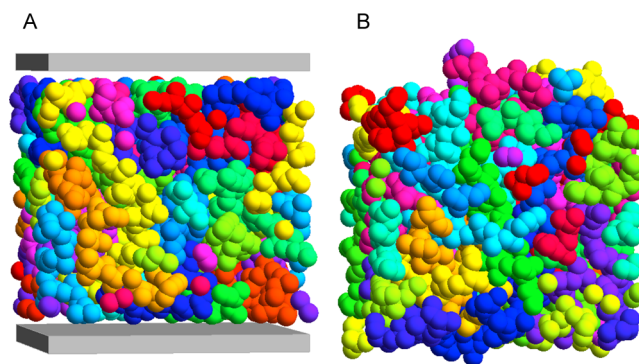


Figure 11. Representative configurations of (A) melt–substrate and (B) melt–vacuum interfaces. Hydrogen atoms have been omitted. Carbons are space filling. Atoms are colored by chain.

interface with the substrate, and had a preferred distance of about 1.7 Å from the substrate. This is again in excellent agreement with the rule of thumb of Israelachvili.³¹ The substrate provides both attractive and repulsive forces that draw atoms to their optimal gap spacing. In contrast, the melt–vacuum interface is more jagged. Chains near the vacuum interface are only restricted in their wandering near the interface by an aversion to leaving the bulk melt.

The surface tension of the melt with vacuum γ_m was 26.1 ± 0.2 erg/cm², and the interfacial tension of the melt with the substrate γ_{ms} was 30.9 ± 0.2 erg/cm² at 400 K. Extrapolation to infinite molecular weight increased the surface tension by 12%. Tail corrections increased the tensions by 9.0 and 12.4 erg/cm², respectively. The tail correction for γ_{ms} was larger because tail corrections to the surface tension are expected to be more significant for sharp interfaces from eq 20.

The value for γ_m deviates by roughly 10% from reported experimental values for γ_m , which have a value of about 23.4 erg/cm².^{33,34} Although some error is obviously introduced by our own approximations, this discrepancy can be partially attributed to the effect of melt polydispersity on the surface tension. In our molecular weight corrections, we analyzed data for fairly monodisperse melts (in particular, the alkane series). Our simulated melt was also monodisperse, and all chains were extrapolated to infinite molecular weight. However, “real” melt polypropylene is polydisperse ($M_w/M_n \approx 4$). Since the surface tension for short chains can be considerably lower than for long chains, we might expect that the experimentally observed surface tension for a polydisperse melt should be somewhat

lower than the surface tension for a monodisperse melt of only long chains.

At first, it might seem surprising that γ_{ms} is larger than γ_m at finite temperature. Intuitively, we might expect that γ_{ms} should be smaller than γ_m because the substrate provides cohesive energy that the vacuum does not, as was the case for the crystal against the surface. However, we know that potential energy is not the only contributor to the surface tension, and that entropic effects can be important. The substrate restricts the motion of chains near the interface in a significant way for the melt that it cannot for the crystal because the crystal is already rigidly structured. The substrate forms an impenetrable surface from which all chains are obligated to turn back, while the vacuum forms only a weak boundary in which chains are free to wander. Chains near the substrate are also densely packed in an attempt to get the most cohesive energy possible from the substrate. Thus, we expect the entropic penalty for the melt-substrate interface to be considerably larger than for the melt-vacuum interface at finite temperature.

Contact Angle. With estimates for γ_{xs} and γ_{ms} at typical crystallization temperatures, we may make an estimate for the contact angle of the crystal nucleus against the Hamaker constant matched surface. Assuming Young's equation is a reasonable estimate for the contact angle θ (10.1021/ma400702q), the contact angle θ is

$$\theta = \cos^{-1} \left(\frac{\gamma_{ms} - \gamma_{xs}}{\gamma_{(s)}} \right) \quad (24)$$

where $\gamma_{(s)}$ is the interfacial tension of the melt with the lateral face of the nucleus. Note that since both γ_{ms} and γ_{xs} include γ_s , the estimation of this value does not impact the value of the contact angle. We have previously estimated the value of $\gamma_{(s)}$ to be 15.9 ± 3.6 erg/cm² (10.1021/ma400702q).

Given these values, the contact angle is estimated to be $79 \pm 3^\circ$. This value for θ is in reasonable agreement with the values for the contact angle extracted from experimental data, which ranged from 40 to 70° with a mean of 56° (10.1021/ma400702q). The discrepancy between the two may be partially attributed to error incurred by the harmonic approximation at finite temperature, our estimation of $\gamma_{(s)}$, assumptions about the nature of the substrate, and errors in the Hamiltonian. Regardless of the exact value of the contact angle, it is important to emphasize that the most significant result of our calculation is that it is plausible for the nucleus to partially wet the substrate, and that the contact angle for this partial wetting should be acute, as we have consistently found in our analysis of experimental data.

CONCLUSION

We have successfully calculated interfacial free energies for crystalline isotactic polypropylene. As Lacks and Rutledge found previously, quantum vibrational free energy contributed significantly due to increased vibrations by atoms near the surface. Tail corrections made a significant contribution to the surface free energy, but did not much affect the Hessian matrix (and thus the vibrational energy) and so could be added as a postsimulation correction. We were able to simulate sufficiently large systems that finite slab size effects were not significant.

Similarly, we were able to simulate the interfacial tensions of polypropylene melt against vacuum and a substrate. The interfacial tension with the substrate was larger than the melt surface tension, likely due to greater loss of translational

entropy near the substrate. Tail corrections proved to be significant for the melt, and molecular weight corrections increased the interfacial tension by 12% from the simulated value.

Modeling of the crystal slab against a Hamaker constant matched surface predicted a contact angle of $79 \pm 3^\circ$, which is in reasonable agreement with the value previously extracted from experimental data. This provides evidence that the cylindrical cap model for heterogeneous nucleation is reasonable. In future work, the surface energy at finite temperature may be treated more carefully with the quasi-harmonic approximation to predict more accurate values for the contact angle.

APPENDIX: TAIL CORRECTIONS

It is our objective to evaluate the tail correction for material in a slab beyond the volume already accounted for within the cutoff radius r_c

$$\Delta U_{ij} = \frac{\rho_j}{2} \int_{V_c} d\mathbf{r}_{ij} U(|\mathbf{r}_{ij}|) \quad (25)$$

Since this integral is not simple to evaluate, we will do this by adding and subtracting simpler integrals. Suppose that we have a slab of thickness $2d$ which is periodic in two dimensions and has gaps in the third dimension. Choose any atom i in the slab. This atom will have distances h_1 and h_2 to the edge of the slab ($h_1 \leq h_2$). If we assume $r_c \leq d$, Figure 12 shows three possible

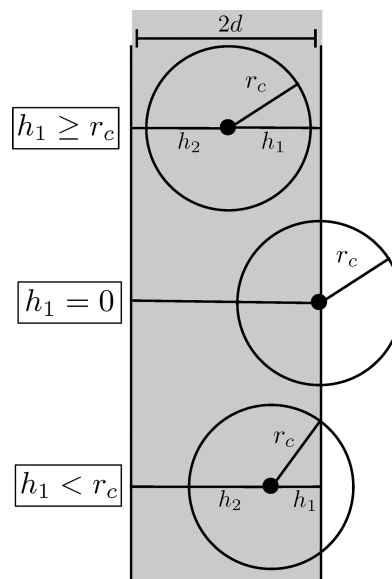


Figure 12. Sketch of cutoff scenarios for an atom in a slab with cutoff radius r_c , thickness $2d$, distances to edges h_1 and h_2 ($h_1 \leq h_2$), and full periodicity in other dimensions.

scenarios for the atom's position. Enforcing that $r_c \leq d$ somewhat simplifies the problem by guaranteeing that the cutoff sphere does not exit both sides of the slab (a fourth scenario). The optimal choice for r_c is d (about 19 Å for our system) since this effectively removes the first scenario; only a marginal number of atoms would fall into the category of being exactly d from the edge. For all cases, we will follow a general scheme of (1) adding back a full spherical tail correction as if the system were homogeneous, (2) subtracting for material which is not present in the slab dimension, and (3) adding back

any material which was incorrectly subtracted because it lies within the cutoff radius.

For the first case ($h_1 \geq r_c$), eq 25 can be evaluated by taking the full spherical integral, and subtracting the interaction with two semi-infinite half planes in the slab dimension

$$\Delta U_{ij} = U_{\text{sph}}(r_c) - U_{\text{half}}(h_1) - U_{\text{half}}(h_2) \quad (26)$$

where $U_{\text{half}}(h)$ is found by integrating over a semi-infinite domain and is given by eq 12.

The second case where the atom lies exactly on the boundary is also easily solved in this manner. Since the atom lies exactly on the boundary, we cannot use the same correction as in the first case, since $U_{\text{half}}(0)$ diverges. However, we can instead consider only a hemisphere tail correction and then subtract a single semi-infinite half plane to obtain the missing energy

$$\Delta U_{ij} = \frac{1}{2} U_{\text{sph}}(r_c) - U_{\text{half}}(2d) \quad (27)$$

The nontrivial case occurs when the distance to the boundary is less than the cutoff radius. As before, we add back a full spherical tail correction, and subtract two semi-infinite half planes. However, this removes some interactions that were never calculated in simulation since they lie inside the cutoff radius (more specifically inside a spherical cap), so this energy must be restored. The energy of the cap is found by integrating in spherical coordinates

$$U_{\text{cap}}(r_c, h) = \frac{\rho_j}{2} \int_0^{\phi'} d\phi \int_{r(\phi)}^{r_c} dr U(r) 2\pi r^2 \sin \phi \quad (28)$$

where $\cos \phi' = h/r_c$ and $r(\phi) = h/\cos \phi$ are the necessary limits of integration in this geometry. Carrying out this integration gives the result in eq 13. Then, the complete tail correction is

$$\Delta U_{ij} = U_{\text{sph}}(r_c) - U_{\text{half}}(h_1) - U_{\text{half}}(h_2) + U_{\text{cap}}(r_c, h_1) \quad (29)$$

Finite Thickness Correction

Suppose that we have a slab of thickness $2d$ sufficiently thick that a continuum approximation is valid for atoms a distance d away. It is our goal to extend the slab to “infinite” thickness (Figure 13). We first separate the slab into two half slabs of thickness d (step 1). Then we can add a continuum slab of thickness L to the middle (step 2). If we let h_i be the nearest edge distance for the i th atom with a specific atom type, then

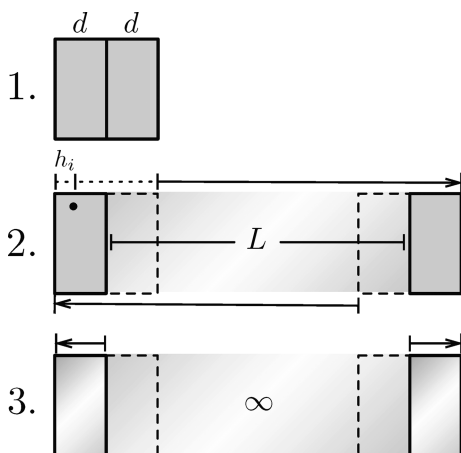


Figure 13. Schematic of finite thickness correction.

we can add the energy of each atom interacting with this slab by integrating the Lennard-Jones potential. If the total added thickness is L , then the atom is “missing” energy from a distance $2d - h_i$ away to a distance $2d - h_i + L$ away (indicated by arrows). This is because we have already calculated the potential in the first $2d - h_i$. Then, the correction $\Delta U_{L,i}$ is

$$\Delta U_{L,i} = \frac{\rho_j}{2} \int_{2d-h_i}^{2d-h_i+L} dz \int_0^\infty dr U(\sqrt{r^2 + z^2}) 2\pi r \quad (30)$$

However, we want to expand the added slab to infinite thickness, so letting L tend to infinity, we find that $\Delta U_{L,i}$ simply becomes $U_{\text{half}}(2d - h_i)$.

Currently, our correction is described in terms of discrete atom positions h_i . However, if d is large, then the half slabs may also be treated as a continuum. The correction term to the surface energy is half of the cohesive energy per unit area of interface, which is equivalent to the energy in one of the half slabs per area (step 3). Integrating through this half slab gives the correction term to the surface tension per unit area for density of type i in the half plane interacting with type j in the added infinite plane.

$$\begin{aligned} \Delta \gamma_{xs|ij} &= \rho_i \int_d^{2d} dh U_{\text{half}}(h) \\ &= \frac{\pi}{2} \rho_i \rho_j \epsilon_{ij} \left[\frac{\sigma_{ij}^{12}}{90} \left(\frac{1}{d^8} - \frac{1}{(2d)^8} \right) - \frac{\sigma_{ij}^6}{3} \left(\frac{1}{d^2} - \frac{1}{(2d)^2} \right) \right] \end{aligned} \quad (31)$$

Then, the correction term to the surface tension is

$$\Delta \gamma_{xs} = \sum_{i,j}^{\text{types}} \Delta \gamma_{xs|ij} \quad (32)$$

where the sum is taken over all possible atom types for the half plane and the added infinite plane.

Effect of Tail Corrections on Hessian

As stated in the text, given a large enough cutoff radius, we can analyze the effect of tail corrections on the normal modes by analyzing the magnitude of tail corrections to the Hessian matrix. We require two important criteria: (1) that the cutoff radius is large enough that a continuum approximation is valid and (2) all atoms are at their positions corresponding to the “true” energy minimum.

A cutoff radius of 1.0 nm is large enough that all important short-ranged interactions are treated discretely, and a continuum approximation beyond the cutoff is valid. Although we have expanded the cutoff radius to 1.9 nm and approximated with continuum beyond this cutoff when computing the tail corrections, we could have also simply approximated with continuum beyond the original 1.0 nm with minimal loss of accuracy.

It is also important that the Hessian is computed around the “true” position of atoms at the energy minimum. If the atoms are not at their “true” minimum, the Hessian may not accurately represent the system. The tail correction in the bulk crystal is constant, so the atoms have no additional forces. We state without proof (for now) that the forces in the slab system are negligibly small, so we may reasonably assume that the atoms are at their “true” minimum energy positions. This

statement will be justified later. It is thus valid to analyze corrections to the Hessian by considering only the second derivatives of the tail corrections.

By definition, the (i,k) th entry in the Hessian is

$$H_{ik} = \frac{\partial^2 U}{\partial x_i \partial x_k} \quad (33)$$

where i and k are indexes corresponding to atom number and the coordinate axis of differentiation. Since tail corrections are additive, the tail correction to the Hessian ΔH_{ik} is

$$\Delta H_{ik} = \frac{\partial^2 \Delta U}{\partial x_i \partial x_k} \quad (34)$$

where ΔU is the total tail correction of either the bulk or slab system

$$\Delta U = \sum_i^N \sum_j^n \Delta U_{ij} \quad (35)$$

and N is the number of atoms and n is the number of density types. For the bulk system, ΔU_{ij} is a constant term independent of atom position (U_{sph}), and so ΔH_{ik} will be zero.

The tail corrections in the slab system, on the other hand, have a position dependence. From eq 11, the correction on the i th atom is decoupled from other atoms and varies only in a single dimension, so ΔH_{ik} will be zero for all $i \neq k$ and for all dimensions that are not the slab dimension. This amounts to correcting one-third of the diagonal elements of the Hessian.

Taking two derivatives in the slab dimension is equivalent to taking two derivatives with respect to the nearest edge distance h_i , and eliminates all atoms in ΔU except for the i -th atom. Analyzing the dominant term of ΔU_i shows that

$$\Delta U_i \sim \begin{cases} n\epsilon\rho\sigma^6 h/r_c^4 & h \leq r_c \\ n\epsilon\rho\sigma^6/h^3 & h > r_c \end{cases} \quad (36)$$

where ϵ and σ are “typical” Lennard-Jones parameters, ρ is the “typical” density, and h is the nearest edge distance. This implies that

$$\Delta H_{ii,x} \sim \begin{cases} 0 & h \leq r_c \\ n\epsilon\rho\sigma^6/h^5 & h > r_c \end{cases} \quad (37)$$

where the subscript x attempts to clearly indicate that this correction is only necessary for the slab dimension. So, of the one-third of diagonal elements that could be corrected, only those atoms that are far from the edge will have a non-zero correction. The maximum correction will occur for atoms that are r_c from the edge, where $\Delta H_{ii,x} \sim n\epsilon\rho\sigma^6/r_c^5$.

The effect of the tail correction to the Hessian can be analyzed by comparing the magnitude of the correction to the Lennard-Jones term in the Hessian $H_{ii|LJ}$. Because of Lennard-Jones 1–4 exclusions, we expect only attractive terms so

$$U_{ii|LJ} \sim \frac{\epsilon\sigma^6}{r^6} \quad (38)$$

Taking two derivatives and summing shows

$$H_{ii|LJ} \sim \frac{N\epsilon\sigma^6}{r^8} \quad (39)$$

where N is the number of atoms inside the cutoff radius (but outside the 1–4 exclusions). The characteristic radius for these interactions must be on the order of σ . For the rough purpose of scaling, the number of atoms in that shell for a cutoff radius of a few σ should be

$$N \sim n\rho r^2 \Delta r \sim n\rho\sigma^3 \quad (40)$$

in a continuum sense, so $H_{ii|LJ} \sim n\epsilon\rho\sigma$. Comparing the two terms

$$\frac{\Delta H_{ii,x}}{H_{ii|LJ}} \sim \left(\frac{\sigma}{r_c}\right)^5 \ll 1 \quad (41)$$

Therefore, the tail correction to these elements of the Hessian is negligible, and we may be reasonably confident that the normal modes are accurate.

Note that this analysis was predicated on the assumption that r_c was sufficiently large to accurately capture the short-ranged interactions. If r_c became small, our scaling shows that these corrections would no longer be negligible. Moreover, for large r_c the correction will actually decay faster (like $1/r_c^6$ when $r_c \gg \sigma$).

We have previously stated that forces due to tail corrections in the slab dimension are negligibly small. By a similar argument to the Hessian, the force corrections in the periodic dimensions are zero and

$$\Delta F_{i,x} \sim n\epsilon\rho\sigma^2 \left(\frac{\sigma}{r_c}\right)^4 \ll 1 \quad (42)$$

in the slab direction, so these derivatives are indeed negligible and the atoms may be assumed to be at their “true” minimum.

AUTHOR INFORMATION

Corresponding Author

*(M.P.H.) E-mail: mphoward@princeton.edu.

Notes

The authors declare no competing financial interest.

ACKNOWLEDGMENTS

The authors acknowledge support from NSF DMR-0907376 and ACS PRF 49964-ND7.

REFERENCES

- (1) Silvestre, C.; Di Lorenzo, M.; Di Pace, E. Crystallization of Polyolefins. In *Handbook of Polyolefins*, 2nd ed.; Vasile, C., Ed.; Taylor & Francis: New York, 2000.
- (2) Lacks, D.; Rutledge, G. *J. Phys. Chem.* **1994**, *98*, 1222–1231.
- (3) Lacks, D.; Rutledge, G. *Macromolecules* **1995**, *28*, 1115–1120.
- (4) Lacks, D.; Rutledge, G. *J. Chem. Phys.* **1994**, *101*, 9961–9965.
- (5) Wilhelm, J. L.; Rutledge, G. C. *J. Phys. Chem.* **1996**, *100*, 10689–10695.
- (6) Zhao, H.; Tang, Z.; Li, G.; Aluru, N. *J. Appl. Phys.* **2006**, *99*, 064314.
- (7) Kirkwood, J.; Buff, F. *J. Chem. Phys.* **1949**, *17*, 338–343.
- (8) Chapela, G.; Saville, G.; Thompson, S.; Rowlinson, J. *J. Chem. Soc., Faraday Trans. 2* **1977**, *73*, 1133–1144.
- (9) Alejandre, J.; Tildesley, D.; Chapela, G. *Mol. Phys.* **1995**, *85*, 651–663.
- (10) Blokhuis, E.; Bedeaux, D.; Holcomb, C.; Zollweg, J. *Mol. Phys.* **1995**, *85*, 665–669.
- (11) Israelachvili, J. In *Intermolecular and Surface Forces*, 2nd ed.; Academic Press: Amsterdam, 1992; Chapter 15.

- (12) Hess, B.; Kutzner, C.; van der Spoel, D.; Lindahl, E. *J. Chem. Theory Comput.* **2008**, *4*, 435–447.
- (13) Jorgensen, W.; Maxwell, D.; Tirado-Rives, J. *J. Am. Chem. Soc.* **1996**, *118*, 11225–11236.
- (14) Frenkel, D.; Smit, B. In *Understanding Molecular Simulation*, 2nd ed.; Academic Press: New York, 2001; Chapter 3, pp 36–37.
- (15) Natta, G.; Corradini, P. *Nuovo Cimento* **1960**, *15*, 40–51.
- (16) Hirose, M.; Yamamoto, T.; Naiki, M. *Comput. Theor. Polym. Sci.* **2000**, *10*, 345–353.
- (17) Ferro, D.; Brückner, S.; Meille, S.; Ragazzi, M. *Macromolecules* **1992**, *25*, 5231–5235.
- (18) Corradini, P.; Petraccone, V.; Pirozzi, B. *Eur. Polym. J.* **1983**, *19*, 299–304.
- (19) Essmann, U.; Perera, L.; Berkowitz, M.; Darden, T.; Lee, H.; Pedersen, L. *J. Chem. Phys.* **1995**, *103*, 8577–8593.
- (20) Bussi, G.; Donadio, D.; Parrinello, M. *J. Chem. Phys.* **2007**, *126*, 014101.
- (21) Alejandre, J.; Tildesley, D.; Chapela, G. *J. Chem. Phys.* **1995**, *102*, 4574–4583.
- (22) LeGrand, D.; Gaines, G., Jr. *J. Colloid Interface Sci.* **1969**, *31*, 162–167.
- (23) Sauer, B.; Dee, G. *Macromolecules* **1991**, *24*, 2124–2126.
- (24) Li, C.; Choi, P. *J. Phys. Chem. B* **2006**, *110*, 6864–6870.
- (25) Thompson, R. B.; MacDonald, J. R.; Chen, P. *Phys. Rev. E* **2008**, *78*, 030801(R).
- (26) Wu, S. In *Polymer Interface and Adhesion*; Marcel Dekker: New York, 1982; Chapter 3.
- (27) *DIPPR Project 801*; Design Institute for Physical Property Research/AICHE, <http://dippr.byu.edu>: 2013.
- (28) Lide, D., Ed. *CRC Handbook of Chemistry and Physics*, 88th ed.; CRC Press: New York, 2007.
- (29) Rubinstein, M.; Colby, R. In *Polymer Physics*; Oxford University Press: Oxford, U.K., 2003; Chapter 2.
- (30) Krygier, E.; Lin, G.; Mendes, J.; Mukandela, G.; Azar, D.; Jones, A.; Pathak, J.; Colby, R.; Kumar, S.; Floudas, G.; Krishnamoorti, R.; Faust, R. *Macromolecules* **2005**, *38*, 7721–7729.
- (31) Israelachvili, J. In *Intermolecular and Surface Forces*, 2nd ed.; Academic Press: Amsterdam, 1992; Chapter 11.
- (32) Vega, C.; de Miguel, E. *J. Chem. Phys.* **2007**, *126*, 154707.
- (33) Roe, R. J. *J. Phys. Chem.* **1968**, *72*, 2013–2017.
- (34) Wu, S. In *Polymer Handbook*, 4th ed.; Brandrup, J., Immergut, E., Grulke, E., Eds.; Wiley-Interscience: New York, 2003; Chapter VI.